

ratios of decay rates:

$$\frac{\Gamma(\bar{B}^0 \rightarrow [f]_D \bar{K}^{*0}) + \Gamma(B^0 \rightarrow [f]_D K^{*0})}{\Gamma(\bar{B}^0 \rightarrow [f]_D \bar{K}^{*0}) - \Gamma(B^0 \rightarrow [f]_D K^{*0})} \quad (1)$$

$$\frac{\Gamma(\bar{B}^0 \rightarrow [f]_D \bar{K}^{*0}) - \Gamma(B^0 \rightarrow [f]_D K^{*0})}{\Gamma(\bar{B}^0 \rightarrow [f]_D \bar{K}^{*0}) + \Gamma(B^0 \rightarrow [f]_D K^{*0})} \quad (2)$$

r_S is the ratio between opposite- and same-sign

δ_S resonance has a natural width ($50 \text{ MeV}/c^2$) larger than the experimental resolution. This introduces a phase difference between the various amplitudes therefore introduce effective variables r_S, k, δ_S , obtained by integrating over the region of the $\bar{D}^0 K^+ \pi^-$ Dalitz plot dominated by the K^{*0} , defined as follows:

$$r_S \equiv \frac{\Gamma(B^0 \rightarrow D^0 K^+ \pi^-)}{\Gamma(B^0 \rightarrow \bar{D}^0 K^+ \pi^-)} = \frac{\int dp A_u^2(p)}{\int dp A_c^2(p)} \quad (3)$$

$$\delta_S \equiv \frac{\int dp A_c(p) A_u(p) e^{i\delta(p)}}{\sqrt{\int dp A_c^2(p) \int dp A_u^2(p)}} \quad (4)$$

For definition, $0 \leq k \leq 1$ and $\delta_S \in [0, 2\pi]$. The amplitudes for the $b \rightarrow c$ and $b \rightarrow u$ transitions (A_c, A_u), are real and positive and $\delta(p)$ is the strong phase. The variable p indicates the position in the $K^+ \pi^-$ Dalitz plot. The parameter k accounts for contributions, in the K^{*0} mass region, of higher-mass resonances. In the case of a two-body B decay, r_S and δ_S are $r_B = A_u/A_c$ and δ_B (the strong phase difference between A_u and A_c) with $k = 1$. As shown in Figure 2, the distribution of k can be obtained by simulation based on realistic models for the different resonances contributing to the decays of neutral B mesons into $\pi^+ \pi^\pm$ final states. When considering the region $\bar{D}^0 K^+ \pi^-$ Dalitz plane where the invariant mass of the kaon and the pion is within $48 \text{ MeV}/c^2$ of the K^{*0} mass [7], the distribution of k is narrow, centered at 0.95 with a root-mean-square width of



error control. In practice, the goodness of fit is used to monitor the quality of the reconstructed data ($h(t) = \delta l/l$) was estimated after, this is assumed as a systematic error in the model and the expected GW signal for long GRB progenitors is the so-called collapse of a massive star down to a black hole, in a peculiar type of SN-like explosion, the favored scenario for short GRB production. This process is believed to occur entirely over within a few seconds, naturally accretion powers the GRB, both long and short. Unlike with long bursts, there is no convective accretion system ends as a rotating BH and the rotational axis of the system [1] is located within the jet. In the standard model, the edges of the jet are

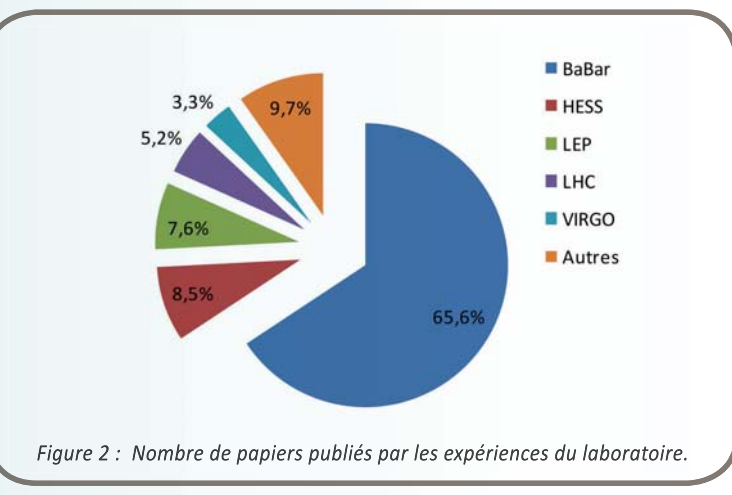
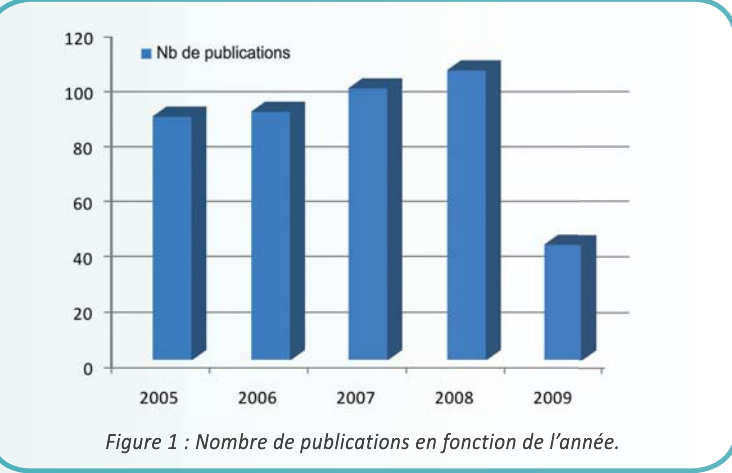
La production scientifique

nario. Fig. 3 presents the mean integrated gamma-ray flux per IMBH for various energy thresholds as a function of the mass of the DM particle annihilating into $b\bar{b}$. Also displayed are the error bars corresponding to the r.m.s. variation of the integrated flux distribution. For a 1 GeV threshold, well suited for gamma-ray satellite experiments, the maximum flux is obtained for a DM particle mass of $\sim 80 \text{ GeV}$. This maximum comes from the balance between the factor $m_\chi^{-9/7}$ and the integral of the annihilation spectrum up to the DM particle mass (see Eq. 6). Adopting an energy threshold of 100 GeV, as appropriate for Cherenkov telescopes such as H.E.S.S., the largest fluxes are obtained for a mass of $\sim 5 \text{ TeV}$. For this mass, the mean of the integrated flux distribution is $4.5 \times 10^{-11} \text{ cm}^{-2} \text{ s}^{-1}$. For masses close to the experimental threshold, the integrated flux increases with the dark matter mass. Well above the threshold, the standard regime is recovered, with fluxes decreasing with m_χ .

Production scientifique

Expérience	2005	2006	2007	2008	2009	Total	Citations	Citations/an	Citations/papier	H index	N citations papier le plus cite
BaBar	61	64	66	62	24	277	3251	650,2	11,8	26	149
HESS	0	1	11	15	9	36	507	126,8	14,1	12	79
Virgo	2	2	3	5	2	14	45	9,0	3,0	4	14
ATLAS	2	2	2	6	1	13	92	18,4	7,7	6	26
CMS	1	0	2	2	1	6	103	20,6	14,7	3	86
AMS	1	1	1	1	1	5	52	10,4	13,0	2	52
Geant 4		1		2		3	224	44,8	74,7	2	194
POLAR	1					1	16	4,0	16,0	1	16
ILC						0					
NOMAD		1	1	1		3	2	0,5	0,7	1	2
GAMS	1		1			2	1	0,2	0,5	1	1
LHCb		2		1		3	9	2,25	3	1	7
MacFly				1	1	2	16	5,33	8	1	16
ALEPH	5	3	3	0	1	12	122	24,4	10,17	5	66
L3	10	5	2	1	0	18	68	13,6	3,78	5	13
LEP	0	2	0	0	0	2	218	54,5	109	2	121
POSITRON	0	1	2	1	0	4	23	5,8	5,8	2	19
UTFIT	0	2	1	1	0	4	118	29,5	29,5	4	51
CKM Fitter	1					1	326	65,2	326	1	326
OPERA	0	1	0	2	1	4	42	10,5	10,5	1	40
ions lourds	1					1	2	0,5	2	1	2
HORS COLLAB	2	2	2	5	1	12	309	61,8	25,75	8	124
TOTAL	88	90	98	105	41	422	5546	13,142	34	326	

Nombre de publications par expérience dans des revues avec comité de lecture, indices de citation et H index.



Production scientifique

Nous passons en revue ici les publications du laboratoire. Pour ce qu'il suit seulement les papiers publiés avec comité de lecture ont été considérés. Dans le tableau suivant, on trouvera pour les années 2005 à juin 2009 le nombre de publications de référence internationale par expérience avec leur indice H ainsi que le nombre de citations. Toutes ces données proviennent de web of sciences.

Le laboratoire publie en moyenne environ 90 à 100 papiers par an et ceci depuis plusieurs années, voir la Figure 1. La Figure 2 montre la contribution de chaque expérience au nombre total des publications. Elle reflète la fin des expériences au LEP, l'expérience BaBar en pleine production scientifique, et les nouveaux thèmes émergents. Le nombre de papiers démontre le succès des expériences et les bon choix stratégiques du laboratoire.